Solar Energy Materials & Solar Cells 267 (2024) 112732

Contents lists available at ScienceDirect

Solar Energy Materials and Solar Cells

journal homepage: www.elsevier.com/locate/solmat

Structural, optical, and photo-electrochemical properties of Aurivillius-type layered $Bi_4Ti_3O_{12}$–$BiFeO_3$ oxides

Elisa Mercadelli [*], Nicola Sangiorgi [**], Simone Fabbri, Alex Sangiorgi, Alessandra Sanson

National Research Council of Italy, Institute of Science, Technology and Sustainability for Ceramics, (CNR-ISSMC, former ISTEC), Via Granarolo 64, 48018, Faenza, Italy

ARTICLE INFO

Keywords:
Aurivillius
Perovskites
Bismuth ferrite
Bismuth titanate
Synthesis
Photo-electrochemistry

ABSTRACT

Photo-electrochemical cells (PECs) represent one of the most promising technologies today for storing sun energy as chemical bonds (solar fuels), exploiting carbon dioxide as a starting reagent. However, identifying suitable photoelectrodes remains a challenging and open issue. In this work, the possibility of using Aurivillius-type compounds to produce solar fuels was deeply investigated. Aurivillius-type perovskites, with general formula $Bi_{(n+1)}Fe_{(n-3)}Ti_3O_{(3n+3)}$ (BFTO-n), were synthesized and fully characterized to study the influence of the number of perovskite layers and the synthesis parameters on their final properties. Specifically, eight different systems were considered increasing the amount of iron and, consequently, the number of perovskite layers. These compounds were synthesized through both a standard solid-state reaction method and a sol-gel technique. For each system, a screen printing ink was formulated to be deposited as photo-electrodes onto transparent conducting supports, and their morphological (XRD and SEM analysis) electrochemical and photo-electrochemical properties (cyclic and linear voltammetry, impedance, Mott-Schottky analysis) were determined. The obtained results demonstrate the potentiality of Aurivillius-type compounds as innovative materials for carbon dioxide photo-electrochemical reduction.

1. Introduction

Aurivillius-type layered ferroelectric ceramics have garnered growing interest in the last two decades. This is attributed to their interesting electrical properties as lead-free piezoelectrics operating at high temperatures and to their great potential for tailoring specific properties by varying their chemical composition and number of layers [1].

Among the others, $Bi_{n+1}Fe_{n-3}Ti_3O_{3n+3}$ (BFTO-n) Aurivillius phases within the binary $Bi_4Ti_3O_{12}$–$BiFeO_3$ system, are naturally formed by perovskite slabs, composed by n $(Bi_{n+1}Fe_{n-3}Ti_3O_{3n+1})^{2-}$ layers stacked along the [001] direction, and separated by $(Bi_2O_2)^{2+}$ fluorite-type layers (Fig. 1). These layered compounds combine ferroelectric, magnetic and magneto-electric properties, making them potentially attractive as multiferroic materials for information processing and storage applications [2].

More interestingly, BFTO-n systems have been also considered as potential multifunctional photocatalysts due to several interesting characteristics. The visible-light absorption is enhanced by the presence of Bismuth that pushes up the valence band edge thanks to the hybridization of Bi 6s with O 2p orbital. This effect may also improve the mobility of the photo-generated holes favoring chemical reactions [3]. In addition, their polarization may be effective in promoting the separation of photo-generated electrons and holes.

Among the available bismuth-based photocatalysts, bismuth titanate $Bi_4Ti_3O_{12}$ (BTO, formed by 3 perovskite layers) has recently drawn growing interest as an abundant, stable, and highly-photocatalytic-active compound [4], due to its peculiar crystal and electron structure [5]. On this basis, several BTO-based powder systems have been successfully reported over the years, for multiple photocatalytic purposes [6–8], and recently BTO has been employed as catalyst also in the CO_2 photo-reduction reactions [9,10]. $Bi_4Ti_3O_{12}$ has been also applied as bifunctional piezo-photocatalysts in Rhodamine B degradations reaction [11]. The piezo-photocatalytic property of this material prepared by molten salt method in nanoplates form, was used to enhance the dye degradation by reducing the charge recombination. Moreover, it was recently found that the piezoelectric properties of BTO can be enhanced by different doping approaches and chemical elements [12]. The

* Corresponding author.
** Corresponding author.
E-mail addresses: elisa.mercadelli@cnr.it (E. Mercadelli), nicola.sangiorgi@cnr.it (N. Sangiorgi).

https://doi.org/10.1016/j.solmat.2024.112732
Received 17 November 2023; Received in revised form 24 January 2024; Accepted 28 January 2024

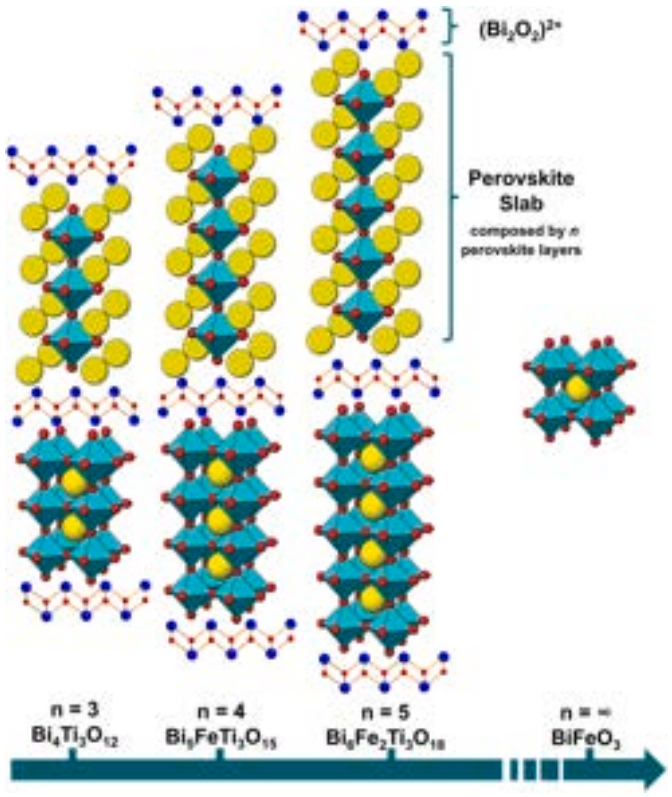

Fig. 1. Sketch of the Aurivillius structures.

influence of oxygen vacances on the photoelectrochemical properties of BTO photoelectrodes prepared by spin coating was recently investigated. After argon treatment, the photocurrent at 0.5 V vs Ag/AgCl was enhanced by 4.4 times compared to bare BTO due to an abundant presence of oxygen vacancies that reduces recombination and increase carrier injection rate as demonstrated by electrochemical impedance spectroscopy and photoluminescence measurements [13].

On the other hand, a lot of work has been published on $BiFeO_3$ (the structure composed ideally by infinite perovskite layers) focusing on the study and development of poled ferroelectric photo-electrodes for water splitting reactions, carbon dioxide conversion, piezophotocatalysis, and photo-electrochemical applications [14–18]. $BiFeO_3$ prepared by one step hydrothermal synthesis has been recently tested in photo-catalytic hydrogen generation achieving hydrogen production of 216 μmol g^{-1} h^{-1} under 450 W Hg lamp with cutoff filter >380 nm and TEOA as sacrificial agent [19]. $BiFeO_3$ photo-electrodes were used in water splitting reactions, particularly with $BiFeO_3/Cu_2O$-based heterojunction. The photocurrent increased by 6.8 times when the copper oxide layer was deposited on BFO compared to a bare BiFeO3 photoelectrode. This enhancement was attributed to increased light absorption and reduced resistances [20]. Charge separation and transfer (CTS) processes in $BiFeO_3$ nanocrystalline photoelectrodes can be controlled by an external poling applied to a photoelectrode with different positive or negative bias voltage. The correlation between the external poling voltage and surface potential was discovered and CTS was increased by 110 % with a −40 voltage (V) poling to the photoelectrode [21].

Despite their potentialities in visible-light photocatalysis, BFTO-n systems have been investigated so far mainly with a focus on the influence of doping elements (La [22], Ca, Sr, Pb [23], Co [24], Eu [25], etc) and on the morphologies of the BFTO-n nanostructures (microflowers [26,27], nanofibers [28], nanosheet [29], nanoshelves [30]). These studies aim to enhance the photocatalysts performance for water purification, pollutant degradation, air purification, and self-cleaning applications [4].

Besides environmental remediation, visible-light driven photocatalysis has recently received increasing attention in the field of renewable energy generation, for sunlight-assisted water splitting and CO_2 reduction to produce several chemicals or fuels. In particular, the photoelectrochemical reduction of CO_2 by semiconducting photoelectrodes (PEC) seems the most promising approach to obtain chemical fuels [31]. This technology consists in the fabrication of a device in which a suitable photoelectrode, i.e. an electrode coated with a light-sensitive semiconductor, interacts with a liquid electrolyte when exposed to light. In this way, electron-hole pairs are photogenerated driving reduction-oxidation reactions for chemical fuel production.

In this work, BFTO-n systems, with n = 3, 4, 5, 6, 7, 8, 9 up to $BiFeO_3$ (n = ∞), will be synthesized and fully characterized for the first time to be implemented as photo-electrodes for photo-electrochemical (PEC) applications. Two different synthetic routes will be considered: sol-gel synthesis and solid-state reaction. The influence of the number of perovskite layers of BFTO-n series on optical, morphological, electrochemical and photo-electrochemical properties will be deeply investigated.

2. Experimental

2.1. Synthesis of the powders

The 8 systems considered in this work and reported in Table 1 were synthesized via two different methods.

For the solid-state reaction route, the stoichiometric amount of Bi_2O_3 (99.999 %, Sigma Aldrich, Germany), Fe_2O_3 (>96 %, Sigma Aldrich, Germany) and TiO_2 (20:80 % rutile:anatase, 99.9 %, Evonik, Germany) were calculated following the reaction:

$$(0.5x+2)Bi_2O_3 + (0.5x)Fe_2O_3 + 3TiO_2 \rightarrow Bi_{(n+1)}Fe_{(n-3)}Ti_3O_{(3n+3)}$$

where n = x+3.

The oxide precursors were ball milled in ethanol (>99.8 %, Sigma Aldrich, Germany) for 24 h, dried and sieved at 150 μm. The precursor mixture was then calcined at 900 °C × 12 h (except for BFO, which was calcined at 850 °C × 12 h for stability issues), to obtain the pure phase and finally sieved again at 150 μm. The powders obtained throughout this method, will be named as "SOLID".

For the sol-gel method, the stoichiometric amount of $Bi(NO_3)_3{\cdot}5H_2O$ (98 %, Sigma Aldrich, Germany), $Fe(NO_3)_3{\cdot}9H_2O$ (99.95 % Sigma Aldrich, Germany) and $Ti(OCH(CH_3)_2)_4$ (97 %, Sigma Aldrich, Germany) were calculated following the reaction:

$$(n+3)Bi(NO_3)_3 + (n-3)Fe(NO_3)_3 + 3Ti(OiPr)_4 \rightarrow Bi_{(n+3)}Fe_{(n-3)}Ti_3O_{(3n+1)}$$

where n is the number of perovskite layers.

The sol-gel synthesis procedure used in this work is schematized in Fig. 2.

In a typical procedure to produce a 5 g-batch, the stoichiometric amount of Fe and Bi nitrate were dissolved in 80 ml of Ethylen glycol (99.8 %, Sigma Aldrich, Germany) and Acetic acid (glacial, 99.99, Sigma Aldrich, Germany) solution. The stoichiometric amount of Ti

Table 1
Chemical formula of the BFTO-n systems considered in this work, number of perovskite layers (n) and stoichiometric coefficient (x).

Sample	Formula	n	x Bi	x Fe	x Ti
BTO-3	$Bi_4Ti_3O_{12}$	3	2	0	3
BFTO-4	$Bi_5FeTi_3O_{15}$	4	2.5	0.5	3
BFTO-5	$Bi_6Fe_2Ti_3O_{18}$	5	3	1	3
BFTO-6	$Bi_7Fe_3Ti_3O_{21}$	6	3.5	1.5	3
BFTO-7	$Bi_8Fe_4Ti_3O_{24}$	7	4	2	3
BFTO-8	$Bi_9Fe_5Ti_3O_{27}$	8	4.5	2.5	3
BFTO-9	$Bi_{10}Fe_6Ti_3O_{30}$	9	5	3	3
BFO	$BiFeO_3$	–	0.5	0.5	0

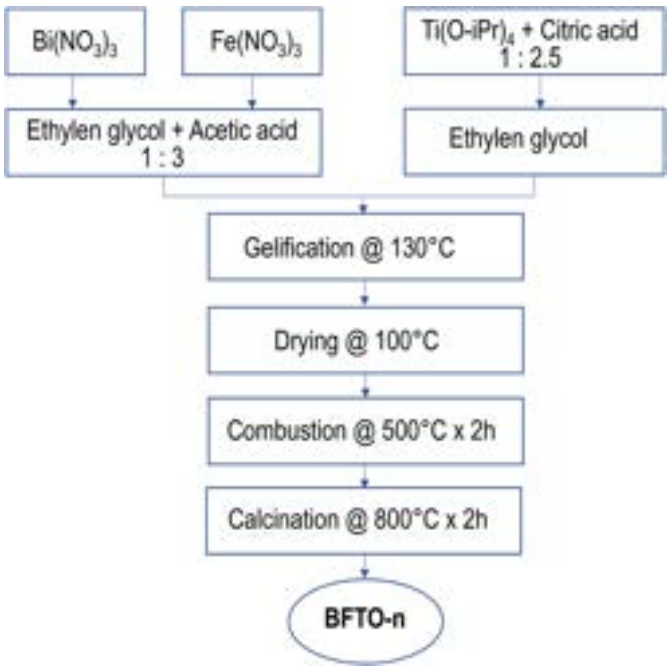

Fig. 2. Synthesis procedure used to obtain BFTO-n "SOLGEL" systems.

isopropoxide was dissolved in 100 ml of Ethylen glycol using citric acid as chelating agent. The as-prepared solutions were then mixed and heated at 130 °C under magnetic stirring up to the gel formation. The latter was then dried at 100 °C for 16 h, pre-treated at 500 °C to remove the organics, and finally calcined at 800 °C to obtain the BFTO-n powders (named as SOLGEL).

2.2. Powder characterization

The BFTO-n powders were characterized by X-ray diffraction (Bruker D8 Advance, Karlsruhe, Germany). XRD patterns were recorded, using Cu Kα radiation at room temperature, in the 5–80° 2θ measuring range, with an equivalent counting time of 92.5 s per 0.02° 2θ step.

The powders morphology was investigated by scanning electron microscopy (SEM-FEG, Carl Zeiss Sigma NTS GmbH, Oberkochen, Germany).

The band-gap energy of BFTO-n powders was calculated from UV–Vis spectra through the Tauc equation [32]:

$$\alpha h\upsilon = A\left(h\upsilon - E_g\right)^{1/n}$$

where α is the absorption coefficient, h is the Planck's constant (J·s), ν is the light frequency (s^{-1}), A is the absorption constant and E_g is the band gap energy value, using n = 1/2 for a direct band gap material as reported in literature [33].

2.3. Fabrication of the photoelectrode

For each BFTO-n system prepared, a suitable screen printing ink was produced. Two inks formulations were considered: for BTO-3, BFTO-4 and BFTO-5, for which, the titanium amount is higher than the Fe one, the ink was formulated (Table S1) following previous works [34,35]. On the other hand, for BFTO-6, BFTO-7, BFTO-8, BFTO-9, BFO, a composition similar to the one reported in Ref. [36] was used (Table S1 of the Supplementary Material). The inks were produced mixing the BFTO-n powders with terpyneol (>96 % Sigma-Aldrich, Germany) as solvent, lauric acid (>96 % Sigma-Aldrich, Germany) or phospholan PE65 (Specialities s. r.l.) as deflocculant, ethyl cellulose (EC 46, Sigma-Aldrich) as binder, and eventually glycerol (>99.5 % Sigma-Aldrich, Germany) as plasticizer. The as-obtained formulations were homogenized in a three-roll mill equipped with zirconia rollers of nanometric finishing (Exakt 80 E, Exakt). The milling was done in a three-steps procedure reducing the gap between the rolls (down to 1 μm) progressively.

BFTO-n based inks were finally deposited onto conductive glass (FTO, Sigma Aldrich 7 Ω/sq) with a semi-automatic screen printer (AUR'EL 900, AUREL Automation s. p.a., Italy). The screen parameters and the number of each subsequent ink deposition were set to finally obtain a 5–7 μm thick square electrode (10 × 10 mm). After the screen printing process, the layers were dried in IR furnace (Ero Electronic SrL, Italy) in static air at 80 °C for 20 min and thermally treated at 550 °C for 1 h.

2.4. Photoelectrode characterization

The phase composition and the morphology of the BFTO-n films was assessed through XRD and SEM-FEG respectively.

The amount of photocatalyst deposited onto the conductive glass was calculated as weight difference of the substrate before and after the deposition.

The thickness of the films was determined by an interferometric profilometer (Contour GT-K 3D, Bruker, Germany) equipped with a 5 × lens.

The bandgap (E_g) energy of the films was calculated from the transmittance spectra using PVE300 (BENTHAM Instruments Ltd, United Kingdom) and re-elaborated following the Kubelka-Munk theory and the Tauc equation.

The Cyclic and Linear Voltammetry (CV and LSV), Electrochemical Impedance Spectroscopy (EIS) and Flat Band determination by Mott-Schottky (MS) analyses were performed with an electrochemical working station (AUTOLAB PGSTAT302 N + FRA32 M, Metrohm, Italy). A three electrodes cell was used to perform these analyses, with Ag/AgCl (KCl 3.5 M) as reference electrode, a counter electrode of platinum foil and the working electrode formed by the BFTO-n film on the FTO glass (the active area analyzed was set at 1 cm^2). CV analyses were performed in a 1 mM $K_3Fe(CN)_6$ (Sigma Aldrich) and 0.1 M KCl (Sigma Aldrich) electrolyte while the potential was applied in the range between +0.8 V to −0.8 V vs Ag/AgCl, with scan rate of 50 mV s^{-1}. EIS analyses were performed with the same electrolyte in dark condition with applied potential equal to 0 V vs Ag/AgCl and the frequency range was varied between 1 × 10^4 and 0.5 Hz, with signal amplitude of 0.01 V. Before each measurement, the solution was purged with argon for 10 min to remove oxygen. Mott-Schottky (MS) analyses were done in KCl (>98 % Sigma Aldrich) 0.1 M water solution (pH 7) in the potential range between +0.8 V and −0.8 V vs Ag/AgCl (starting from the anodic potential) and in a frequency range between 10 KHz and 0.5 Hz with 10 mV amplitude of the AC signal. The Mott-Schottky plots were obtained at frequency of 1 KHz and the flat-band potential (E_{fb}) was determined using the Mott-Schottky equation. Finally, the photocurrents were determined by LSV under stirring and in dark or light conditions. For the latter, two different configurations were used: "light back" when the light reaches the photo-electrode from the glass side and "light front" when the light reaches the photo-electrode from the film side, as schematized in Fig. S1 of the Supplementary Material. The intensity of 1000 W m^{-2} was calibrated with a reference certified silicon cell (Lot-Oriel). Two different experimental set-ups were considered: the first one in reducing conditions with LSV from 0.2 V to −1.5 V at scan rate of 10 mV s^{-1}, using a 0.1 M $KHCO_3$ (>98 % Sigma Aldrich) solution saturated with CO_2; the second one with an oxidation potential ranging from −0.2 V to 1.5 V at scan rate of 10 mV s^{-1}, with a 0.1 M Na_2SO_4 (Anhydrous, Sigma Aldrich) solution as electrolyte, degassed with N_2. With the same electrolyte, EIS analyses in dark and illuminated conditions (1000 W m^{-2}) were done on the best photoelectrodes both in oxidation and reduction conditions. The same EIS experimental parameters above-mentioned were used with two different potentials applied: +1.5 V vs

Ag/AgCl for oxidation conditions and −1.5 V vs Ag/AgCl for reduction conditions.

3. Results and discussion

3.1. Characterization of BFTO-n powders

The possibility of synthesizing BFTO-n systems through solid-state reaction method has been intensively investigated since the 2000s by the Russian group headed by Gusarov [37–39]. The formation of Aurivillius phases in the Bi_2O_3–TiO_2–Fe_2O_3 system is considered a multistage process. In the early stages, compounds with smaller numbers of perovskite layers in the structure and the perovskite $BiFeO_3$ are formed simultaneously. In the subsequent stage, $BiFeO_3$ is incorporated into a perovskite layer of Aurivillius phase increasing the thickness of the perovskite slab until an Aurivillius structure of a given composition is formed.

The right choice of the thermal treatment is therefore crucial for the obtaining of the Aurivillius phase with the desired number of perovskite layers. The XRD patterns reported in Fig. 3a show that the calcination conditions selected in this work (900 °C × 12 h) are the optimal compromise between precursors activation and the thermal stability of the final compound to finally produce the pure Aurivillius systems. It is in fact demonstrated that the thermal stability of Aurivillius phases is strongly affected by the $BiFeO_3$ amount in the system i.e., the higher is the number of perovskite layers, the lower would be the Aurivillius stability. Only traces of a secondary phase ($BiFe_2O_{4.63}$) were detected for the $BiFeO_3$ perovskite, even in milder calcination conditions (850 °C × 12 h). As reported by Morozov [38] and Monteiro [40] the synthesis of $BiFeO_3$ starting from the oxides mixture always contains impurity by-products. This is attributed to its ability to change its equilibrium composition upon rising temperature, forming $(Bi_{1-x}Fe_x)FeO_3$ solid solutions, as well as to its metastability at temperatures exceeding its peritectic decomposition temperature (~950 °C).

All the XRD diffraction peaks match well to those of corresponding standard powder diffraction patterns (for BTO-3, BTFO-4, BTFO-5, BTFO-6, BFO as indicated in Fig. 3) or are consistent with literature data (for BTFO-7 [41], BFTO-8 [42], and BTFO-9 [43]). Generally, the discernible pattern differences in Aurivillius-type BFTO-n oxides with different perovskite slabs mainly manifest in peaks occurring at 15°–20° and 45°–50° 2Θ ranges [44,45]. A closer examination of the XRD patterns for the BFTO-n "SOLID" systems in Fig. S2 of Supplementary Material reveals that, as the number of perovskite layers (n) increases, the distance between the two peaks in the 47°–48° range gradually enlarges (Fig. S2a). Simultaneously, the peak at 16°–20° shifts towards higher angles (Fig. S2b). Furthermore, the width of the (0 0 2n + 1) reflection peak of the samples (Fig. S2c) tends to increase from BTO-3 to BTFO-9, confirming the formation of Aurivillius-type structures with an increased number of layers [44].

The SEM micrographs reported in Fig. 3b evidence that the BTO-3 powder is constituted by plate-like particles, in the micrometric range, typical of Aurivillius compounds due to the preferential growth of the *ab* crystalline plane [46]. The shape anisotropicity as well as the lamella dimensions of the synthesized powders decrease with an increase in the

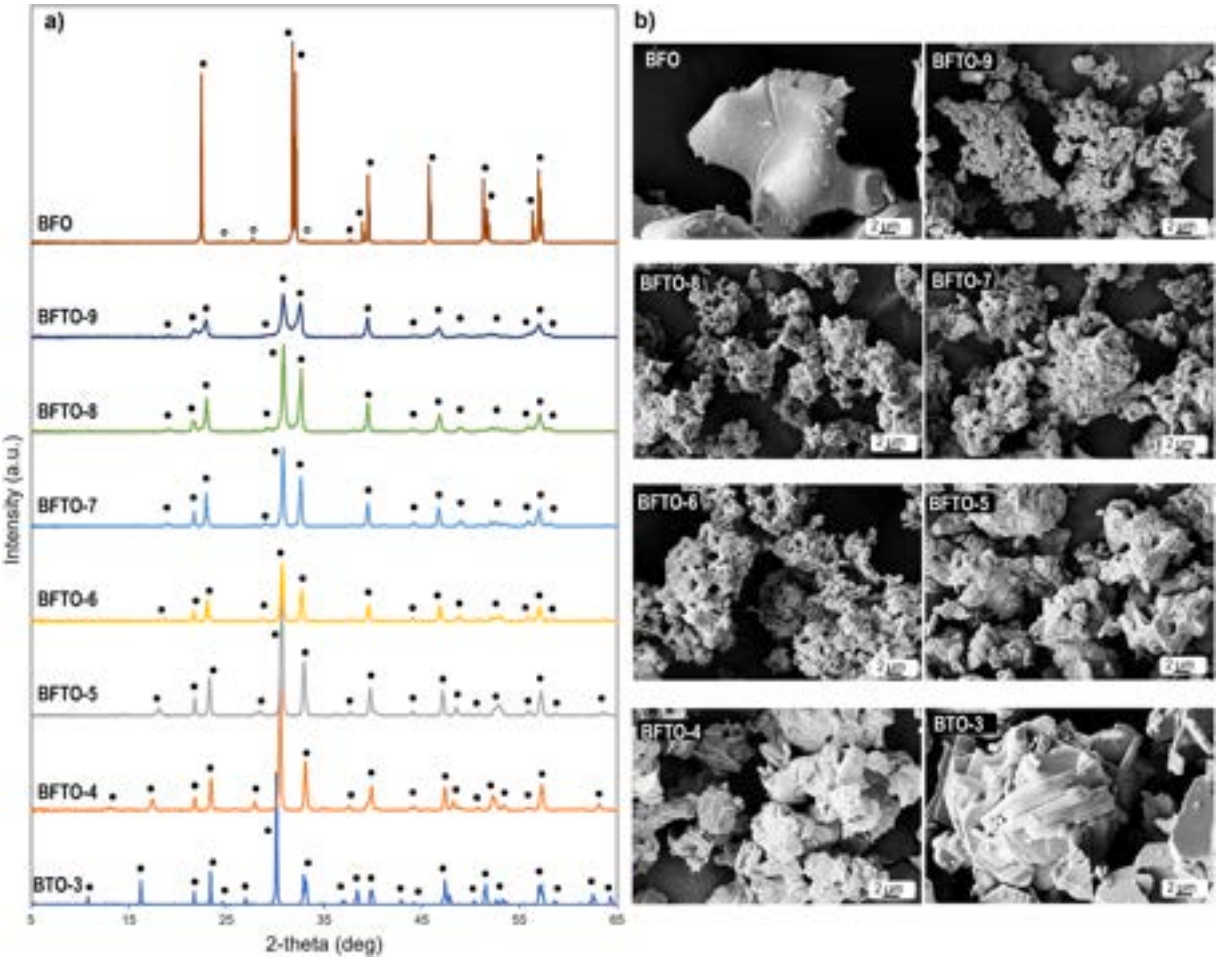

Fig. 3. XRD patterns a) and SEM micrographs b) of BFTO-n "SOLID" systems synthesized through Solid-State Reaction. The diffractograms are indexed as follow: (●) Aurivillius/Perovskite phase (PDF# 35–0795, 82–0063, 75–8378, 54–1044, 66–0439 for BTO-3, BFTO-4, BFTO-5, BFTO-6, BFO respectively), (○) $BiFe_2O_{4.63}$ PDF# 81–9629. Note that PDF cards for BFTO-7, BFTO-8 and BFTO-9 are not available.

number of perovskite layers in the Aurivillius system. The insertion in fact of an increased amount of perovskite layers between the Bi_2O_3 ones, i.e. increasing the distance between the Bi_2O_3 layers, promotes more and more isotropic crystallites growth similarly to a "simple" perovskite. On the other hand, the BFO system is formed by partially sintered polyhedric particles.

The microstructural and morphological characterization of BFTO-n powders produced through sol-gel synthesis is reported in Fig. 4. The XRD results (Fig. 4 a) evidence that the selected synthesis procedure and parameters are suitable to obtain the pure Aurivillius phase, confirming the sol-gel method as a valid tool to obtain a wide range of BFTO-n systems at milder conditions (800 °C × 2 h). All the XRD diffraction peaks match well to those of corresponding standard powder diffraction patterns and are consistent with literature data, as already shown for BFTO-n "SOLID" systems. Only a small trace of a secondary phase was detected for the BFO system.

The morphology of the sol-gel BFTO-n powders (Fig. 4b) is similar to the one obtained by solid-state reaction. The most evident difference is the particles size of the powders, being the former in the sub-micrometric range, due to the higher reactivity of the reactants and, in turn, the lower calcination temperatures.

The band gap values calculated for each synthesized BFTO-n system are graphed in Fig. 5. A direct comparison with literature data is challenging due to the variability in band gap values arising from different synthetic methods. For example, band gap values of 2.96 eV [47], 3.64 eV [48], and 3.1 eV [49], are reported for the BTO-3 systems synthesized

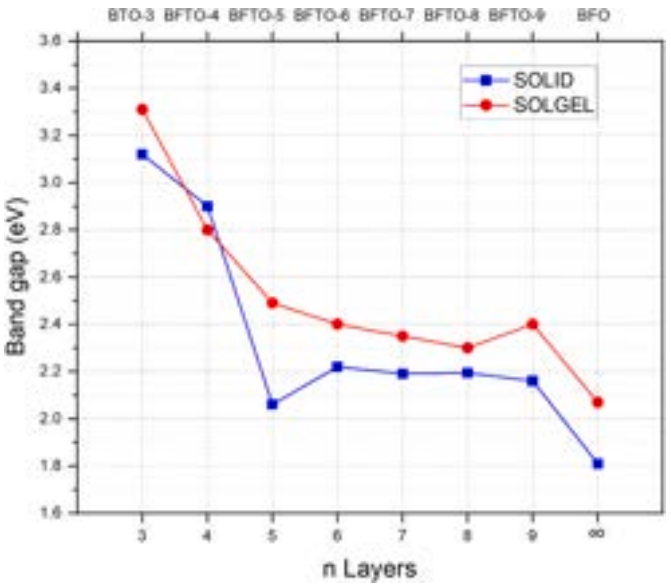

Fig. 5. Band gap values of the synthesized BFTO-n powders correlated to the number of perovskite layers.

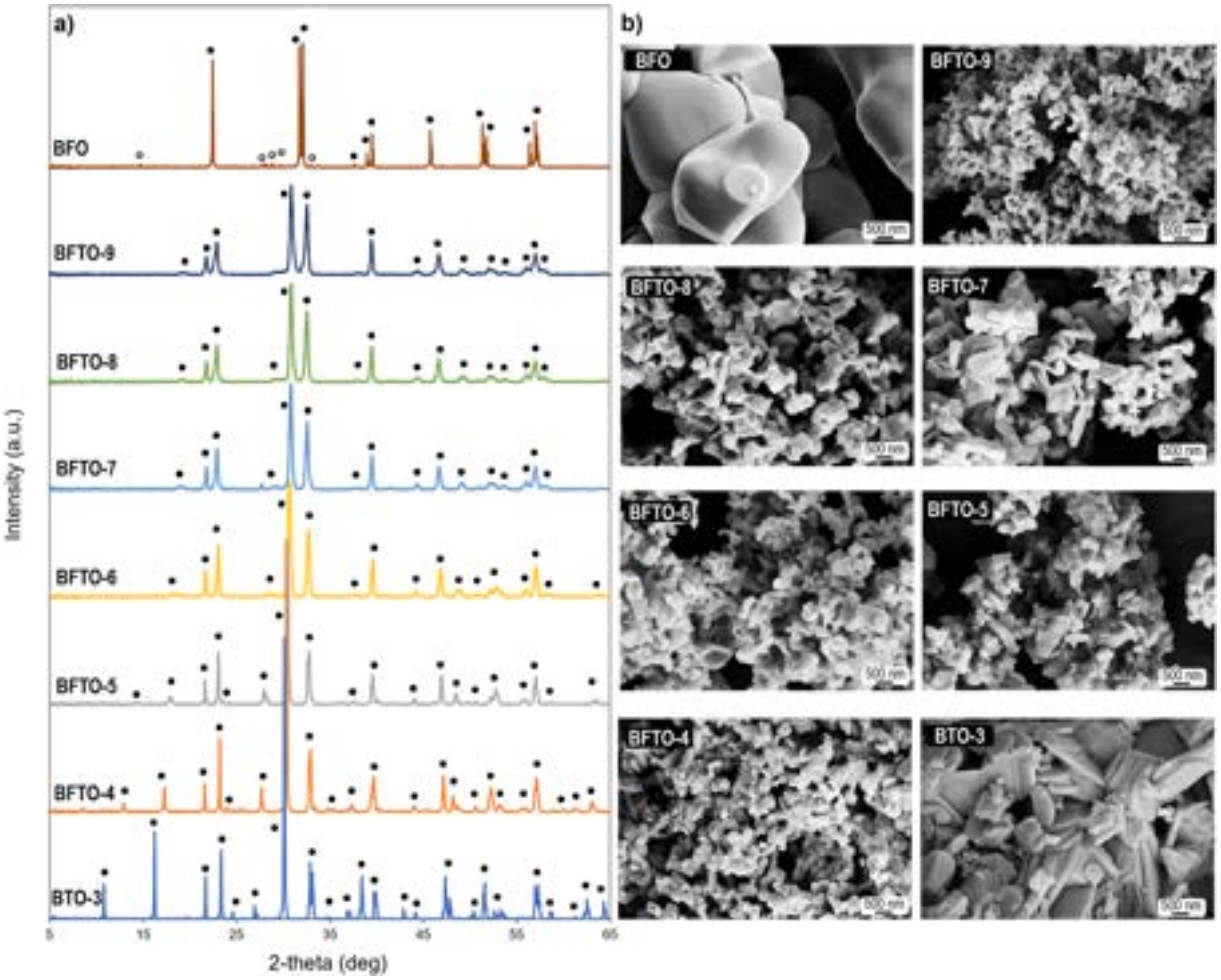

Fig. 4. XRD patterns a) and SEM micrographs b) of BFTO-n "SOLGEL" systems synthesized through the Sol-Gel method. The diffractograms are indexed as follow: (●) Aurivillius/Perovskite phase (PDF# 35–0795, 82–0063, 75–8378, 54–1044, 66–0439 for BTO-3, BFTO-4, BFTO-5, BFTO-6, BFO respectively), (○) $Bi_{24}(Bi_{0.22}Fe_{1.78})O_{39}$ PDF# 84–2562. Note that PDF cards for BFTO-7, BFTO-8 and BFTO-9 are not available.

by chemical synthesis and solid-state reaction respectively, while for BTO-4 values of 3.08 eV [50], 2.39 eV [51], and 2.08 eV [26] are registered for powder synthesized by solid-state reaction and hydrothermal synthesis respectively. On the other hand, Eg values of 3.72 eV for BTO-5 [52], 2.22 eV [30] and 2.04 eV [53] for BTO-6, and 2.5 eV for BFO [54] were reported for systems obtained by chemical methods. It is therefore evident that not univocal band gaps values related to each BFTO-n composition can be found in literature. It is in fact known that these values are strongly influenced by several factors including synthesis method/parameters, crystalline structure, structural defects (i.e. oxygen vacancies), particles size and morphology.

As demonstrated by Fig. 5, the band gap value is affected by the increase in Fe content, in fact the Eg values decrease increasing the perovskite layers number in the BFTO-n structure. The same trend is in fact observed for both the two synthesis methods: systems with a lower number of perovskite layers exhibit higher band gap values, attributed to the higher Ti amount in the crystalline structure (i.e., the Eg value for TiO_2 anatase is 3.2 eV [32]). Conversely, as the number of perovskite layers and the amount of Fe increase, the band gap values decrease (i.e., Eg for Fe_2O_3 is 2.1 eV [55]). However, the data collected suggest that the influence of the Fe amount on the band gap is significant only for a low number of perovskite layers (BFTO-4 and BFTO-5) in respect with the other tested systems (BFTO-6, BFTO-7, BFTO-8, BFTO-9, BFO). Moreover, generally higher band gap values were obtained for the systems synthesized through the sol-gel method. This behaviour is related to the different particle's size and morphology of BFTO-n obtained by the two synthesis methods as reported by the SEM analyses (Figs. 3 and 4). The very low errors associated with each band gap value (Table S2 of the

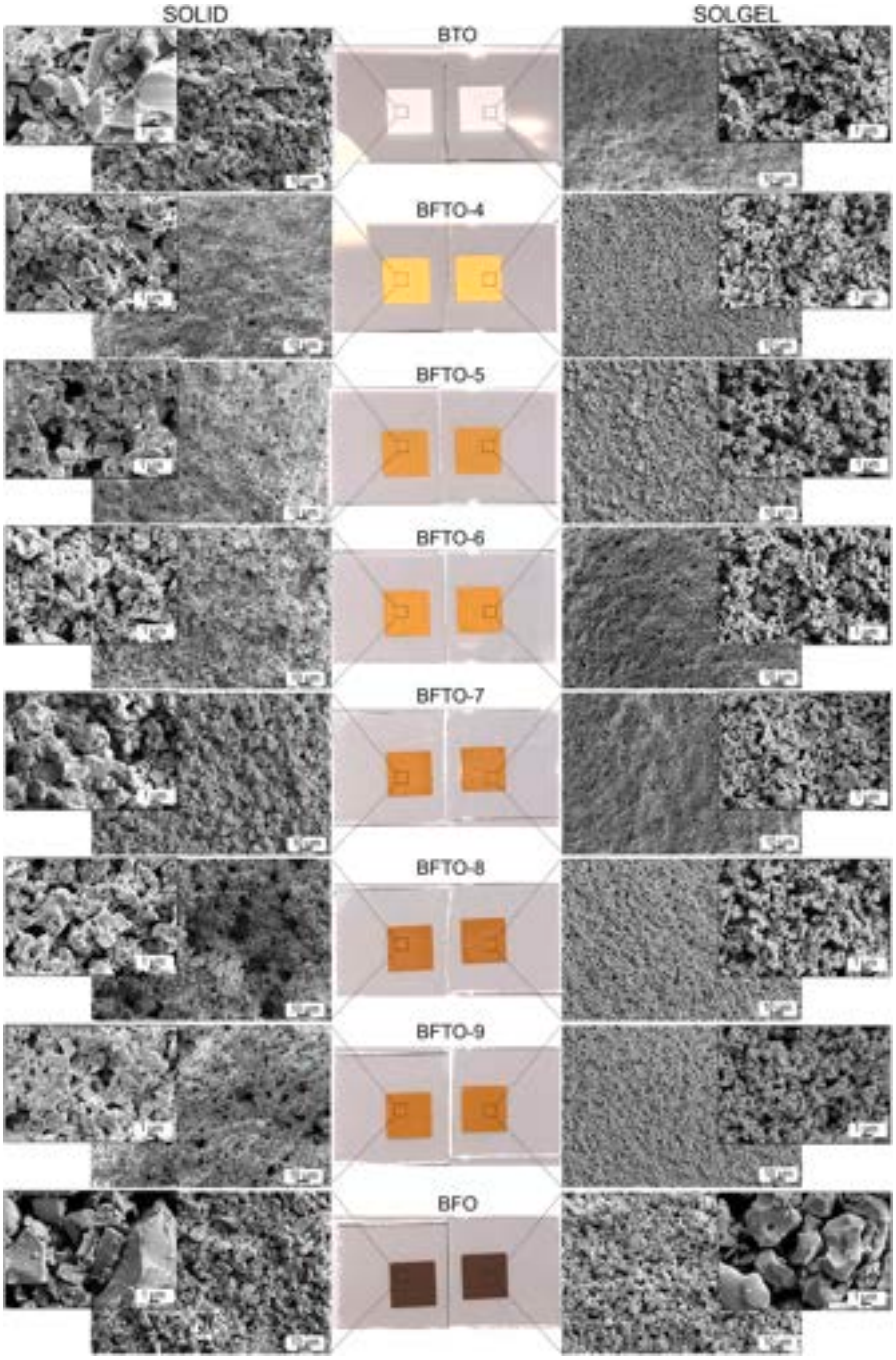

Fig. 6. BFTO-n photoelectrodes screen printed onto conductive glass: photos and SEM micrographs of the surface for each system investigated.

Supplementary Material) indicate good reproducibility of each material and repeatability of the experimental design.

3.2. Characterization of BFTO-n films

Each BFTO-n system was screen printed onto conductive glass following the procedure described in the Experimental section. The optimization of the printing parameters leads to obtain homogeneous cracks-free, and well-adherent electrodes (Fig. 6), with comparable thickness values (5.8 ± 0.6 μm and 5.2 ± 0.5 μm for SOLID and SOLGEL samples respectively) and masses (2.8 ± 0.3 mg and 2.4 ± 0.3 mg for SOLID and SOLGEL samples respectively) of the deposited BFTO-n systems. Moreover, no structural modifications after the screen-printing process were detected through XRD analysis (Fig. S3 of the Supplementary Material).

The SEM micrographs reported in Fig. 6 indicate the absence of superficial defects or microcracks on the surface of the BFTO-n electrodes. Specifically, the films composed of "SOLID" BFTO-n powders exhibit a more heterogeneous morphology, characterized by pores with dimensions up to 10 μm. On the other hand, a more homogeneous and finer porosity was attained in the "SOLGEL" systems. Moreover, the SEM analysis confirms that the particles morphology of the deposited systems is not affected by the processing steps needed to fabricate the electrodes. The same lamella-like particles are in fact found for the BTO-3 systems while globular and polyhedral morphologies are detected for the highest number of perovskite layers and BFO respectively. Nevertheless, a disaggregation effect of the synthesized powders occurs due to the mixing treatment through the three-roll mill during the inks preparation as evident from a comparison of the SEM micrographs in Figs. 3, 4 and 6.

The band-gap values for each BFTO-n film were calculated and reported in Fig. 7. Comparable Eg values were obtained for the "SOLID"- and "SOLGEL"-derived films decreasing from 2.97 ± 0.02 eV–2.99 ± 0.02 eV for BTO-3 systems to 1.87 ± 0.02 eV-1.62 ± 0.04 eV for BFO systems (as previously observed and discussed for as-synthesized powders, Fig. 5). These results confirm the films' capability to absorb visible light and therefore their suitability to be used for photo-electrocatalytic applications.

The electrochemical properties of BFTO-n films were investigated through cyclic voltammetry (CV, Fig. 8) on the $K_3Fe(CN)_6$ oxidation and reduction reactions. Bare FTO electrode CV response was reported for comparison. The graphs show the presence of two main peaks in oxidation and reduction conditions due to the redox activity of the

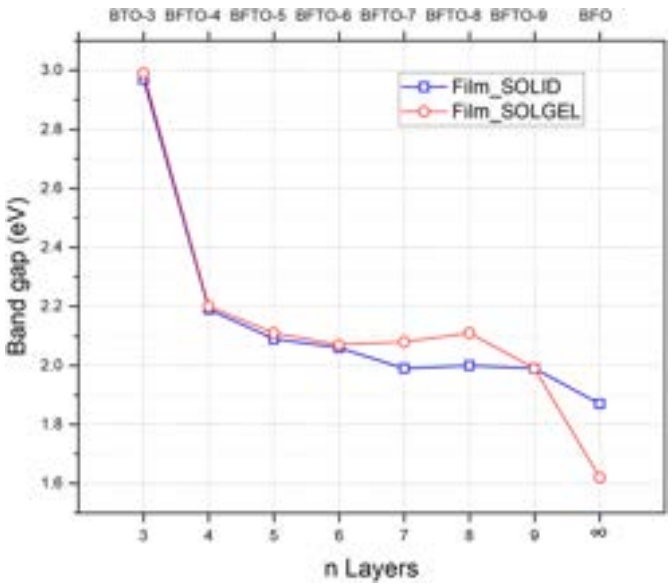

Fig. 7. Band gap values of the investigated BFTO-n films.

BFTO-n films on $K_3Fe(CN)_6$ electrolyte. This confirms the materials' ability to transport charges capable of reacting with the redox specie (Fe^{2+}/Fe^{3+}). However, some differences can be noticed comparing the SOLID and SOLGEL systems. The SOLID BFTO-n films from BTO-6 to BFO generate higher exchanged current densities respect to the FTO-glass reference (Fig. 8a). Nevertheless, BTO, BFTO-4, and BFTO-5 exhibit lower current densities compared to the reference, with the BFO film registering the highest current density values. These results suggest that increasing the number of perovskite layers the ability of these photoelectrodes to drive the oxidation and reduction reaction on $Fe^{2+/3+}$ improves thanks to their structural properties and morphologies.

Similar trends were observed for SOLGEL BFTO-n films (Fig. 8b). Specifically, the produced current density is generally incremented increasing the number of perovskite layers. All the tested photoelectrodes showed an enhancement in exchanged current densities if compared with reference FTO, achieving values higher than the ones registered for the SOLID films. This phenomenon is related to the different morphological characteristics of the films prepared using powders synthesized via two different methods, as previously highlighted by SEM analyses (Fig. 6). It is in fact well known [56,57] that the morphological characteristics, i.e. superficial defects and/or cracks, particles size/morphology, porosity level, and pore size, strongly influence the conductivity and the electrode/electrolyte interaction. SOLGEL BFTO-n films have in fact higher surface area available for improving redox reaction with the electrolyte solution and to increase the electrolyte diffusion.

Finally, it is evident from CV analyses that the smaller particles size of the systems is the predominant factor to enhance redox mechanisms for $Fe^{2+/3+}$ oxidation and reduction reactions and to enhance the electrolyte diffusion in comparison with structural changes of the Aurivillius, i.e. increase of the number of perovskite layers.

The band gap and CV results have clearly demonstrated that the influence of the addition of perovskite layers on the optical and electrochemical properties of BFTO-systems is more significant within the series from BTO-3 to BFTO-5, while between BFTO-6 and BFO is less pronounced. For this reason, the further characterizations will be focused on the systems with n = 3, 4, 5, and BFO.

Electrochemical Impedance Spectroscopy (EIS) measurements were conducted to evaluate the charges mobility and the charge-transfer resistance of the developed materials. Nyquist plots of SOLID and SOLGEL systems are reported in Fig. 9b and c respectively with the equivalent circuit used to fit the experimental points (Fig. 9a). The R_s describes the resistance associated to film adhesion on the substrate and the overall electrical resistance of both material and substrate, while R_{CT} and CPE describe the electrochemical properties of the electrode/electrolyte interface, in particular the charge-transfer resistance and the charge storage capacitance respectively. Fig. 9d and e shows the influence of the number of perovskite layers added into BTO structure on R_S and R_{CT} values respectively.

The Rs values were slightly affected by the increase in the number of perovskite layers. However, considering the absolute values, the electrodes based on powders synthesized by sol-gel method show highest resistance probably due to lower adhesion on the FTO substrate. On the other hand, a clear influence of the number of perovskite layers on R_{CT} was observed. This resistance increases from n = 3 (BTO-3) to n = 4 (BTFO-4) for both sol-gel and solid systems, while R_{CT} decreases rapidly increasing the perovskite layers number (BTFO-5), reaching comparable values for BFO systems. This trend indicates a higher charge-transfer resistance for systems with low number of perovskite layers close to the BTO while increasing n (up to BFO system), the R_{CT} decreases producing more efficient electrodes. As previously observed for band gap values, a clear influence of iron on R_{CT} is registered. The charge-transfer resistance in fact decreases by increasing the iron content due to its higher electrical conductivity than titanium. Finally, EIS analysis shows that the influence of the number of perovskite layers is more crucial on

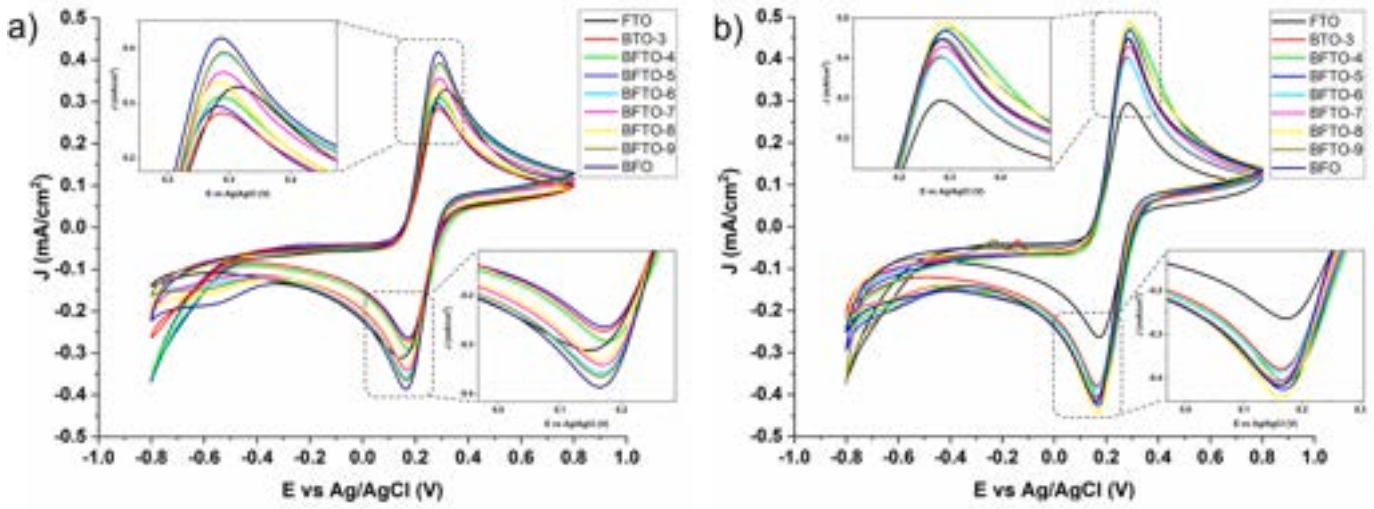

Fig. 8. Cyclic Voltammograms of SOLID a) and SOLGEL b) BFTO-n films acquired at 50 mV s^1 in 1 mM $K_3Fe(CN)_6$ electrolytes.

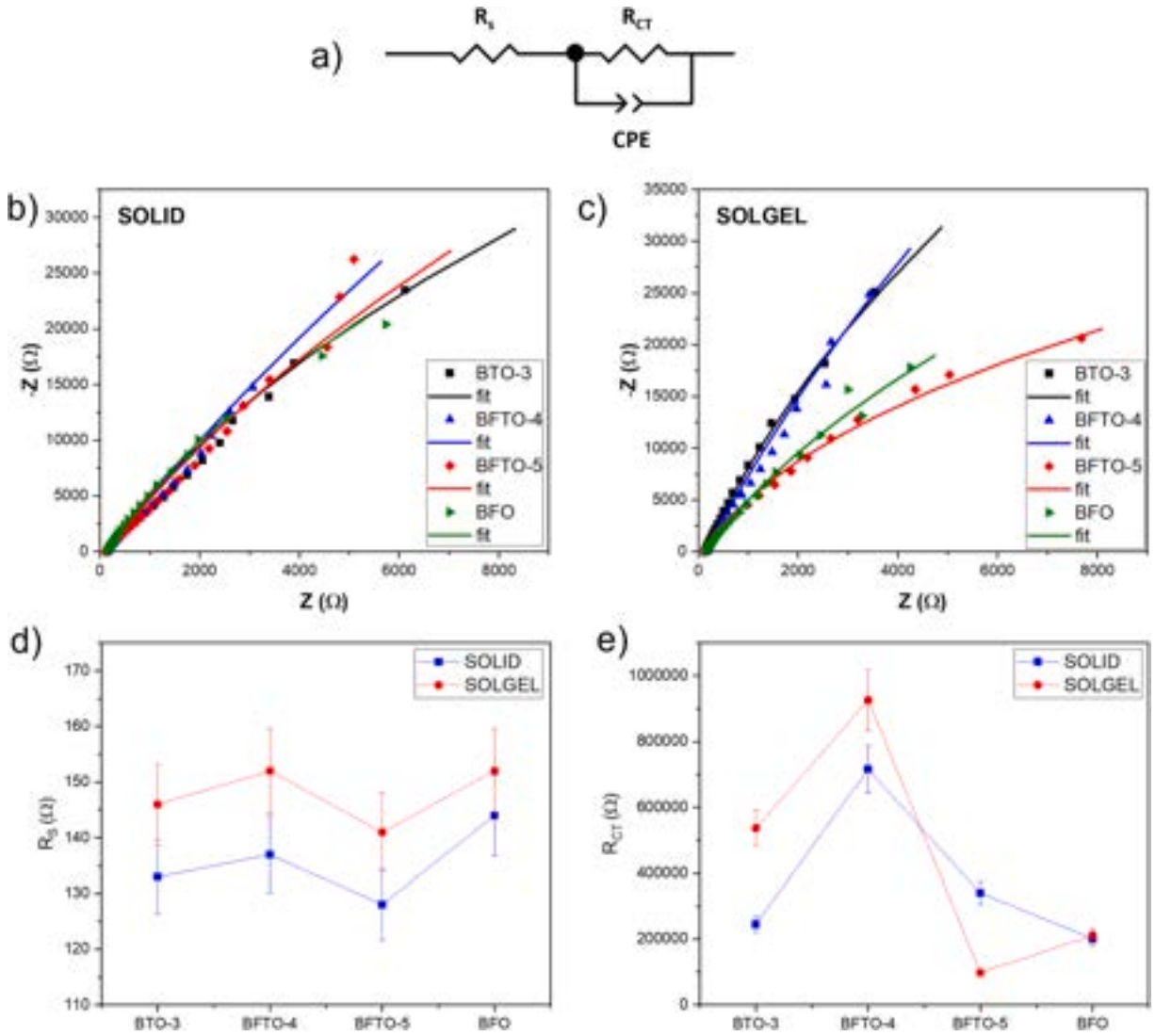

Fig. 9. Nyquist plots and related equivalent circuit (a) for SOLID- (b) and SOLGEL- (c) based photoelectrodes acquired in dark, with applied potential equal to 0 V vs Ag/AgCl in 1 mM $K_3Fe(CN)_6$. R_s (d) and R_{ct} (e) of the investigated BFTO-n films as a function of the number of perovskite layers.

charge transfer resistance especially for higher numbers (n above 4), than on R_s. Perovskite layers are in fact known to be conducting layers while B_2O_2 are insulating ones [58]: the increase of the perovskite layers number coupled with the increased B_2O_2 layers spacing lead to more conductive systems. CV analyses corroborate these results (Fig. 8 shows the highest exchange current densities for photo-electrode with n above 4), confirming the importance of the morphological properties (surface roughness, porosity, particles size/distribution, film adhesion) [56].

The electronic properties and bands position of BFTO-n films were determined using Mott-Schottky analyses (MS). The investigation of these properties is paramount to develop and characterize innovative materials for photo-electrode applications. MS plots are reported in Fig. 10, while Flat-band potentials (E_{fb}) are calculated using the Mott Schottky equation [6]:

$$\frac{1}{C^2} = \frac{2}{\varepsilon\varepsilon_0 e N_A}\left(E - E_{fb} - \frac{k_B T}{e}\right)$$

where C is the specific capacitance (F) extrapolated by the MS plots, ε is the dielectric constant of the material, ε_0 is the dielectric vacuum permittivity (8.85419×10^{-12} C^2 J^{-1} m^{-1}), e is the elementary charge (1.602176×10^{-19} C), N_A is the number of majority charges, E is the applied potential (V), k_B is the Boltzman constant (1.38065×10^{-23} J K^{-1}), and T is the temperature (298 K). The values of E_{fb} were reported in Table S3 of the Supplementary Material. The curves shown in Fig. 10 exhibit positive slopes regardless the synthesis method used, indicating that BFTO-n films are n-type semiconductors, which is consistent with what has been previously reported in the literature [59]. Moreover, the plots reported in Fig. 10 show a different slope for the SOLID and SOLGEL systems. According to Mott-Schottky formula, the slope of M − S curves is inversely proportional to carrier concentration (N_D). As a consequence, the smaller slopes observed for sol-gel synthesized materials compared to those prepared by solid-state reaction indicate an increased number of charges carrier that finally produce a positive effect on photo-electrochemical properties.

The measured E_{fb} vs Ag/AgCl were converted to the normal hydrogen electrode (NHE) scale according to the Nernst equation:

$$E_{NHE} = E_{Ag/AgCl} + 0.059\ pH + E^{\circ}_{Ag/AgCl}$$

where E_{NHE} is the converted potential vs NHE, $E^{\circ}_{Ag/AgCl} = 0.197$ at 25 °C, and $E_{Ag/AgCl}$ is the experimentally measured E_{fb}. For n-type semiconductors, the E_{fb} is generally close to the minimum edge position of the conduction band (CBm). Adding the film bandgap value (Eg) previously calculated, the maximum edge position of Valence Band (VB_M) was calculated [60]. The resulting energy diagrams for SOLID and SOLGEL materials and the standard potential for water splitting and carbon dioxide reduction reactions are plotted in Fig. 11. These data highlight the thermodynamic feasibility of water splitting and of some CO_2 conversion reactions. The potentials of these reactions, in fact, are positioned between the VB and the CB of the BFTO-n films. For BFO electrodes, the CB position is consistent with the one reported in literature [61].

Finally, the BFTO-n films were tested as photo-electrodes in photo-electrochemical cell (PEC), using Linear Scan Voltammetry (LSV) in oxidation and reduction conditions. The corresponding curves are reported in Figs. S4, S5, S6 and S7 of Supplementary Material, while the amounts of current and photocurrent (at potential applied equal to 1.5 V vs Ag/AgCl and −1.5 V vs Ag/AgCl for oxidation and reduction conditions respectively) produced in the different investigated conditions are graphed in Fig. 12. The data demonstrate that all the photo-electrodes are able to generate current or photocurrent in oxidation/reducing conditions and, as a consequence, potentially applicable as both electrocatalysts (dark condition) and photo-electrocatalysts (solar light assisted). However, LSV curves in Figs. S4–S7 show the presence of high recombination phenomena during the illumination conditions due to the high impedance observed for all systems tested (Fig. 9) that reduces the amount of photocurrent achieved. Generally, SOLGEL series with the highest number of perovskite layers (BFTO-5 and BFO) are capable to generate the highest amount of current and photocurrent. This is attributed to the highest amount of charge carriers, as observed from M − S analyses (Fig. 10), combined with smaller particles size in respect with SOLID systems. Under oxidation condition, the best results show photocurrents of 0.04 mA cm^{-2} and 0.02 mA cm^{-2} (at 1.5 V vs Ag/AgCl), achieved by BFO prepared by solgel and solid-state respectively. Moreover, values of 2.71 mA cm^{-2} and 0.64 mA cm^{-2} (at −1.5 V vs Ag/AgCl) were obtained in reduction condition for BFO prepared by solgel and solid-state respectively. In particular, for both oxidation and reduction reactions, the highest photocurrents were achieved in back illumination condition (the light reaches the BFTO-n films from the glass side) thanks to the photogeneration of carriers at the FTO/photo-electrode interface. In fact, in the opposite condition of light front illumination, the photo-generated charges recombine very fast and, consequently, are less available to drive oxidation and reduction reactions. Considering the LSV in oxidation condition, a clear influence of the photo-electrodes chemical composition is observed in particular for SOLGEL systems: the produced currents and photo-currents, in fact, increase up to BFTO-5 and then decrease for BFO, following the same trend of iron content in their chemical structure (Table 1). Considering

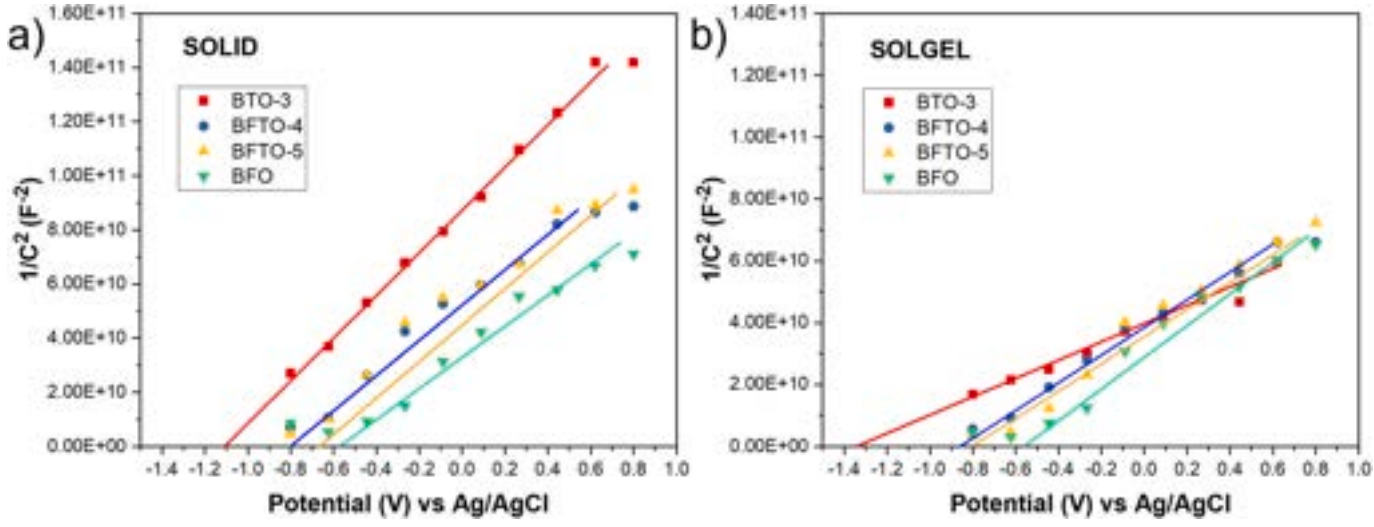

Fig. 10. Mott-Schottky plots (1000 Hz) of SOLID a) and SOLGEL b) BFTO-n films. The solid lines represent the data fitting of the linear part of the curve.

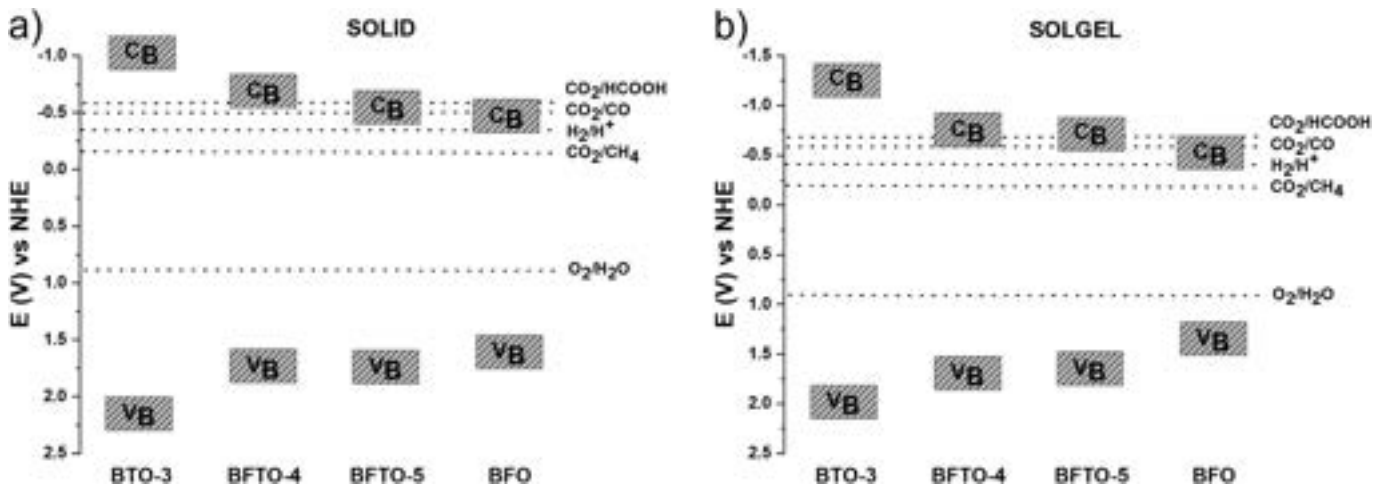

Fig. 11. Energy diagram of SOLID a) and SOLGEL b) BFTO-n films compared to standard potentials of the most common CO_2 reduction processes and water splitting (at pH = 7).

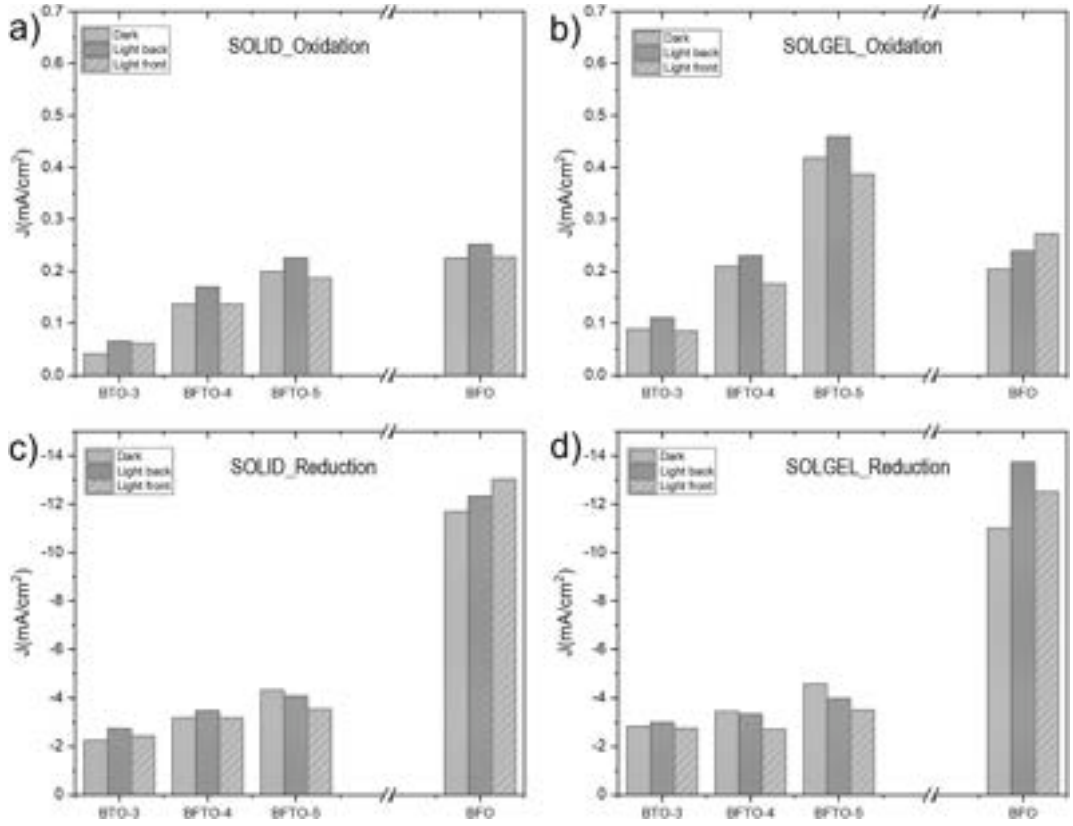

Fig. 12. Current and photocurrent obtained from LSV curves in dark and illumination conditions at potential applied equal to 1.5 V vs Ag/AgCl (a, b) and −1.5 V vs Ag/AgCl (c,d).

LSV in reduction condition, increasing the number of perovskite layers enhances the currents and photo-currents produced due to the n-type conductivity of BFTO-n films that allows a more efficient electrons mobility.

To gain a more detailed understanding of the highest photocurrent produced by BFTO-5 SOLGEL under oxidation conditions and by BFO SOLGEL under reduction conditions, EIS in dark and illumination conditions (1000 W m^{-2}, light back that represents the highest efficient illumination condition) were conducted. The obtained Nyquist plots and the equivalent circuit used to fit the experimental points are reported in Fig. 13. The elements of the equivalent circuit describe the electrical resistance (R_S), the charge-transfer resistance (R_{CT}) at the electrode/electrolyte interface and the capacitance to accumulate charges (CPE).

For BFTO-5 photoelectrode tested in oxidation conditions (Fig. 13a), a higher impedance with respect of BFO was found (both in dark and illumination) confirming the lowest photocurrent produced in this condition (see Fig. 12b). On the other hand, BFO shows a lower impedance compared to BFTO-5 (Fig. 13 b) in reduction condition, corroborating the data reported in Fig. 12d. Furthermore, Fig. 13 confirms that both photoelectrodes can absorb light and effectively transfer photo-generated charges to the electrolyte under different applied voltages. In fact, for BFTO-5 the Rct value decreases from 6246 Ω in dark

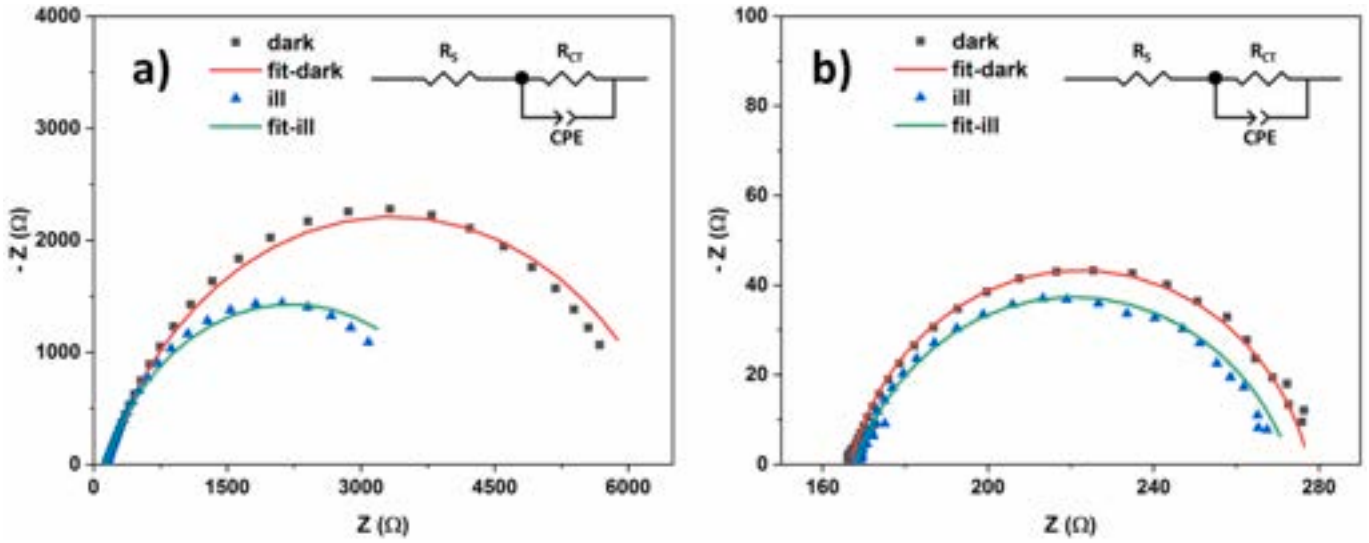

Fig. 13. Nyquist plots of BFTO-5 SOLGEL in oxidation condition (a) and BFO SOLGEL in reduction condition (b).

to 4161 Ω under illumination, while for BFO Rct decreases from 111 Ω to 101 Ω. Moreover, the base of CPE element directly linked to the related electrode/electrolyte interface capacitance increases under illumination for both photoelectrodes. This indicates a higher amount of photo-generated charges available on the film surface. In particular, for BFTO-5 the value of the base of CPE increases from $1.34 \times 10^{-4}\ \Omega^{-1}s^n$ (n is the CPE exponent) to $2.30 \times 10^{-4}\ \Omega^{-1}s^n$ in the dark and under illumination respectively, while for BFO from $1.45 \times 10^{-5}\ \Omega^{-1}s^n$ to $1.94 \times 10^{-5}\ \Omega^{-1}s^n$.

4. Conclusions

A clear influence of the number of perovskite layers on morphology, structural and optical properties in Aurivillius-based BFTO-n (n = 3 for $Bi_4Ti_3O_{12}$ to n = infinite $BiFeO_3$) materials was determined. Increasing the number of perovskite layers decreases the band gap energy from about 3.0 eV to 1.9 eV for BTO and BFO systems respectively. At the same time, the influence of two different synthetic routes on the above-mentioned properties was assessed considering solid-state reaction and sol-gel method. The latter produces powders with small particle size and the correspondent photo-electrodes show the highest electrochemical properties, amount of charge carriers and reduced charge transfer resistances. Moreover, it was found that the electrochemical and photo-electrochemical properties can be modulated changing the number of perovskite layers inside the Aurivillius structure. The most substantial differences were registered for the systems with low number of perovskite layers (3–5) while minor impact was observed for the compositions from n = 6 to BFO. Systems with low number of perovskite layers (BTO-3 to BFTO-5) are suitable materials for photo-electrodes application to drive oxidation reactions (i.e. oxygen evolution reaction) in PEC cells. Otherwise, increasing the number of perovskite layers (BFO) a more efficient photo-electrode for reduction reactions (i.e. carbon dioxide reduction) is achieved. Finally, the energy diagrams of BFTO-n films suggest that all the BFTO-n systems considered can be exploited as photo-electrodes for PEC applications.

CRediT authorship contribution statement

Elisa Mercadelli: Writing – original draft, Validation, Supervision, Methodology, Investigation, Data curation. **Nicola Sangiorgi:** Writing – review & editing, Validation, Methodology, Investigation, Data curation. **Simone Fabbri:** Methodology, Investigation, Formal analysis. **Alex Sangiorgi:** Methodology, Formal analysis, Data curation. **Alessandra Sanson:** Supervision, Project administration, Methodology, Conceptualization.

Declaration of competing interest

The authors declare that they have no known competing financial interests or personal relationships that could have appeared to influence the work reported in this paper.

Data availability

Data will be made available on request.

Acknowledgements

The Authors would like to acknowledge Mrs Paola Pinasco for the XRD analyses on both BFTO-n powders and films.

Appendix A. Supplementary data

Supplementary data to this article can be found online at https://doi.org/10.1016/j.solmat.2024.112732.

References

[1] A. Moure, Review and perspectives of Aurivillius structures as a lead-free piezoelectric system, Appl. Sci. 8 (2018) 62, https://doi.org/10.3390/app8010062.
[2] S. Sun, X. Yin, Progress and perspectives on aurivillius-type layered ferroelectric oxides in binary Bi4Ti3O12-BiFeO3 system for multifunctional applications, Crystals 11 (2021) 23, https://doi.org/10.3390/cryst11010023.
[3] N. Tian, C. Hu, J. Wang, Y. Zhang, T. Ma, H. Huang, Layered bismuth-based photocatalysts, Coord. Chem. Rev. 463 (2022) 214515, https://doi.org/10.1016/j.ccr.2022.214515.
[4] G.A. Kallawar, D.P. Barai, B.A. Bhanvase, Bismuth titanate based photocatalysts for degradation of persistent organic compounds in wastewater: a comprehensive review on synthesis methods, performance as photocatalyst and challenges, J. Clean. Prod. 318 (2021) 128563, https://doi.org/10.1016/j.jclepro.2021.128563.
[5] Z. Chen, H. Jiang, W. Jin, C. Shi, Enhanced photocatalytic performance over Bi4Ti3O12 nanosheets with controllable size and exposed {001} facets for Rhodamine B degradation, Appl. Catal. B Environ. 180 (2016) 698–706, https://doi.org/10.1016/j.apcatb.2015.07.022.
[6] A. Kumar, G. Sharma, A. Kumari, C. Guo, Mu Naushad, D.-V.N. Vo, J. Iqbal, F. J. Stadler, Construction of dual Z-scheme g-C3N4/Bi4Ti3O12/Bi4O5I2 heterojunction for visible and solar powered coupled photocatalytic antibiotic degradation and hydrogen production: boosting via I−/I3− and Bi3+/Bi5+ redox mediators, Appl. Catal. B Environ. 284 (2021) 119808, https://doi.org/10.1016/j.apcatb.2020.119808.

[7] Z. Liu, Z. Ma, Promoting the photocatalytic activity of Bi4Ti3O12 microspheres by incorporating iron, RSC Adv. 10 (2020) 19232–19239, https://doi.org/10.1039/D0RA03305G.

[8] S. Casadio, A. Gondolini, N. Sangiorgi, A. Candini, A. Sanson, Highly transparent Bi4Ti3O12 thin-film electrodes for ferroelectric-enhanced photoelectrochemical processes, Sustain. Energy Fuels (2022), https://doi.org/10.1039/D2SE01372J.

[9] X. Wang, Y. Wang, M. Gao, J. Shen, X. Pu, Z. Zhang, H. Lin, X. Wang, BiVO4/Bi4Ti3O12 heterojunction enabling efficient photocatalytic reduction of CO2 with H2O to CH3OH and CO, Appl. Catal. B Environ. 270 (2020) 118876, https://doi.org/10.1016/j.apcatb.2020.118876.

[10] C. Zhang, Y. Wang, X. Zhang, R. Wang, L. Kou, J. Wang, R. Li, C. Fan, Millimeter-level nitrogen modified activated carbon spheres assisted Bi4Ti3O12 composites for bifunctional adsorption/photoreduction of CO2, Chem. Eng. J. 417 (2021) 128218, https://doi.org/10.1016/j.cej.2020.128218.

[11] Z. Xie, X. Tang, J. Shi, Y. Wang, G. Yuan, J.-M. Liu, Excellent piezo-photocatalytic performance of Bi4Ti3O12 nanoplates synthesized by molten-salt method, Nano Energy 98 (2022) 107247, https://doi.org/10.1016/j.nanoen.2022.107247.

[12] S. Supriya, Bi4Ti3O12 electroceramics: effect of doping, crystal structure mechanisms and piezoelectric response, J. Korean Ceram. Soc. 60 (2023) 451–461, https://doi.org/10.1007/s43207-023-00290-9.

[13] Y. Cui, P. Dang, F. Wang, P. Yuan, W. Liu, Y. Pu, Effect of oxygen vacancies on photoelectrochemical properties of amphoteric semiconductor Bi4Ti3O12 photoelectrode, Vacuum 210 (2023) 111899, https://doi.org/10.1016/j.vacuum.2023.111899.

[14] S. Wang, F. Nan, Y. Zhou, F. Zheng, Y. Weng, L. You, L. Fang, Enhanced photoelectrochemical performance in BiFeO3/g-C3N4 p–n heterojunction photocathodes with ferroelectric polarization, J. Appl. Phys. 128 (2020) 154101, https://doi.org/10.1063/5.0018856.

[15] X. Wu, H. Li, X. Wang, L. Jiang, J. Xi, G. Du, Z. Ji, Ferroelectric enhanced photoelectrochemical water splitting in BiFeO3/TiO2 composite photoanode, J. Alloys Compd. 783 (2019) 643–651, https://doi.org/10.1016/j.jallcom.2018.12.345.

[16] Y.-L. Huang, W.S. Chang, C.N. Van, H.-J. Liu, K.-A. Tsai, J.-W. Chen, H.-H. Kuo, W.-Y. Tzeng, Y.-C. Chen, C.-L. Wu, C.-W. Luo, Y.-J. Hsu, Y.-H. Chu, Tunable photoelectrochemical performance of Au/BiFeO3 heterostructure, Nanoscale 8 (2016) 15795–15801, https://doi.org/10.1039/C6NR04997D.

[17] W. Ji, K. Yao, Y.-F. Lim, Y.C. Liang, A. Suwardi, Epitaxial ferroelectric BiFeO3 thin films for unassisted photocatalytic water splitting, Appl. Phys. Lett. 103 (2013) 062901, https://doi.org/10.1063/1.4817907.

[18] W. Amdouni, M. Fricaudet, M. Otoničar, V. Garcia, S. Fusil, J. Kreisel, H. Maghraoui-Meherzi, B. Dkhil, BiFeO3 nanoparticles: the "holy-grail" of piezo-photocatalysts? Adv. Mater. 35 (2023) 2301841 https://doi.org/10.1002/adma.202301841.

[19] F. Li, J. Zhou, C. Gao, H. Qiu, Y. Gong, J. Gao, Y. Liu, J. Gao, A green method to prepare magnetically recyclable Bi/Bi25FeO40-C nanocomposites for photocatalytic hydrogen generation, Appl. Surf. Sci. 521 (2020) 146342, https://doi.org/10.1016/j.apsusc.2020.146342.

[20] J. Zhu, Y. He, Y. Yang, Y. Liu, M. Chen, D. Cao, BiFeO3/Cu2O heterojunction for efficient photoelectrochemical water splitting under visible-light irradiation, Catal. Lett. 151 (2021) 382–389, https://doi.org/10.1007/s10562-020-03338-1.

[21] X. Li, Z. Wang, W. Ji, T. Lu, J. You, K. Wang, G. Liu, Y. Liu, L. Wang, Polarization alignment in polycrystalline BiFeO3 photoelectrodes for tunable band bending, ACS Nano 17 (2023) 22944–22951, https://doi.org/10.1021/acsnano.3c08081.

[22] G. Naresh, T.K. Mandal, Excellent sun-light-driven photocatalytic activity by Aurivillius layered perovskites, Bi5–xLaxTi3FeO15 (x = 1, 2), ACS Appl. Mater. Interfaces 6 (2014) 21000–21010, https://doi.org/10.1021/am505767c.

[23] G. Naresh, J. Malik, V. Meena, T.K. Mandal, pH-mediated collective and selective solar photocatalysis by a series of layered Aurivillius perovskites, ACS Omega 3 (2018) 11104–11116, https://doi.org/10.1021/acsomega.8b01054.

[24] X. Li, Z. Zhu, F. Li, Y. Huang, X. Hu, H. Huang, R. Peng, X. Zhai, Z. Fu, Y. Lu, Multifunctional single-phase photocatalysts: extended near infrared photoactivity and reliable magnetic recyclability, Sci. Rep. 5 (2015) 15511, https://doi.org/10.1038/srep15511.

[25] Z. Zhu, X. Li, W. Gu, J. Wang, H. Huang, R. Peng, X. Zhai, Z. Fu, Y. Lu, Improving photocatalysis and magnetic recyclability in Bi5Fe0.95Co0.05Ti3O15 via europium doping, J. Alloys Compd. 686 (2016) 306–311, https://doi.org/10.1016/j.jallcom.2016.06.012.

[26] S. Sun, W. Wang, H. Xu, L. Zhou, M. Shang, L. Zhang, Bi5FeTi3O15 hierarchical microflowers: hydrothermal synthesis, growth mechanism, and associated visible-light-driven photocatalysis, J. Phys. Chem. C 112 (2008) 17835–17843, https://doi.org/10.1021/jp807379c.

[27] J. Chen, Z. Li, T. Chen, D. Sun, L. Liu, M. Liu, Y. Lu, The critical role of alkali cations in synthesizing Bi5FeTi3O15 nanocrystals, J. Mater. Sci. 54 (2019) 1948–1957, https://doi.org/10.1007/s10853-018-2976-y.

[28] W. Gu, W. Zhang, L. Zhu, W. Zou, H. Liu, Z. Fu, Y. Lu, Synthesis of Au@Bi6Fe2Ti3O18 nanofibers and the corona-poling enhanced visible-light-driven photocatalysis, Mater. Lett. 241 (2019) 115–118, https://doi.org/10.1016/j.matlet.2019.01.059.

[29] Y. Liu, G. Zhu, J. Gao, M. Hojamberdiev, R. Zhu, X. Wei, Q. Guo, P. Liu, Enhanced photocatalytic activity of Bi4Ti3O12 nanosheets by Fe3+-doping and the addition of Au nanoparticles: photodegradation of Phenol and bisphenol A, Appl. Catal. B Environ. 200 (2017) 72–82, https://doi.org/10.1016/j.apcatb.2016.06.069.

[30] X. Li, Z. Ju, F. Li, Y. Huang, Y. Xie, Z. Fu, R.J. Knize, Y. Lu, Visible light responsive $Bi_7Fe_3Ti_3O_{21}$ nanoshelf photocatalysts with ferroelectricity and ferromagnetism, J. Mater. Chem. A 2 (2014) 13366, https://doi.org/10.1039/C4TA01799D.

[31] Y. Wang, D. He, H. Chen, D. Wang, Catalysts in electro-, photo- and photoelectrocatalytic CO2 reduction reactions, J. Photochem. Photobiol. C Photochem. Rev. 40 (2019) 117–149, https://doi.org/10.1016/j.jphotochemrev.2019.02.002.

[32] N. Sangiorgi, L. Aversa, R. Tatti, R. Verucchi, A. Sanson, Spectrophotometric method for optical band gap and electronic transitions determination of semiconductor materials, Opt. Mater. 64 (2017) 18–25, https://doi.org/10.1016/j.optmat.2016.11.014.

[33] D. Sando, C. Carrétéro, M.N. Grisolia, A. Barthélémy, V. Nagarajan, M. Bibes, Revisiting the optical band gap in epitaxial BiFeO3 thin films, Adv. Opt. Mater. 6 (2018) 1700836, https://doi.org/10.1002/adom.201700836.

[34] R. Bendoni, E. Mercadelli, N. Sangiorgi, A. Strini, A. Sangiorgi, A. Sanson, Alternative route for the preparation of Zr-doped TiO2 layers for energy and environmental applications, Ceram. Int. 41 (2015) 9899–9909, https://doi.org/10.1016/j.ceramint.2015.04.067.

[35] A. Gondolini, E. Mercadelli, G. Constantin, L. Dessemond, V. Yurkiv, R. Costa, A. Sanson, On the manufacturing of low temperature activated Sr0.9La0.1TiO3-δ-Ce1-xGdxO2-δ anodes for solid oxide fuel cell, J. Eur. Ceram. Soc. 38 (2018) 153–161, https://doi.org/10.1016/j.jeurceramsoc.2017.07.035.

[36] A. Sanson, E. Mercadelli, E. Roncari, R. Licheri, R. Orrù, G. Cao, E. Merlone-Borla, D. Marzorati, A. Bonavita, G. Micali, G. Neri, Influence of processing parameters on the electrical response of screen printed SrFe0.6Ti0.4O3−δ thick films, Ceram. Int. 36 (2010) 521–527, https://doi.org/10.1016/j.ceramint.2009.09.028.

[37] M.I. Morozov, L.P. Mezentseva, V.V. Gusarov, Mechanism of formation of Bi4Ti3O12, Russ. J. Gen. Chem. 72 (2002) 1038–1040, https://doi.org/10.1023/A:1020734312307.

[38] M.I. Morozov, N.A. Lomanova, V.V. Gusarov, Specific features of BiFeO3 formation in a mixture of bismuth(III) and iron(III) oxides, Russ. J. Gen. Chem. 73 (2003) 1676–1680, https://doi.org/10.1023/B:RUGC.0000018640.30953.70.

[39] N.A. Lomanova, V.V. Gusarov, Phase states in the Bi4Ti3O12-BiFeO3 section in the Bi2O3-TiO2-Fe2O3 system, Russ. J. Inorg. Chem. 56 (2011) 616–620, https://doi.org/10.1134/S0036023611040188.

[40] F. Casanova Monteiro, P. de Jesus Cubas, V. Sena Kosera, J.F. Haas Leandro Monteiro, S.T. Fujiwara, Photocatalytic activity of BiFeO3 in pellet form synthetized using solid state reaction and modified Pechini method, J. Photochem. Photobiol. Chem. 367 (2018) 390–396, https://doi.org/10.1016/j.jphotochem.2018.08.051.

[41] Z. Lei, T. Chen, W. Li, M. Liu, W. Ge, Y. Lu, Cobalt-substituted seven-layer Aurivillius Bi8Fe4Ti3O24 ceramics: enhanced ferromagnetism and ferroelectricity, Crystals 7 (2017) 76, https://doi.org/10.3390/cryst7030076.

[42] S.K. Patri, R.N.P. Choudhary, B.K. Samantaray, Studies of structural, dielectric and impedance properties of Bi9Fe5Ti3O27 ceramics, J. Electroceram. 20 (2008) 119–126, https://doi.org/10.1007/s10832-007-9376-z.

[43] N. Lomanova, Synthesis features, thermal behavior, and physical properties of Bi10Fe6Ti3O30 ceramic material, Mater. Chem. Phys. 263 (2021) 124386, https://doi.org/10.1016/j.matchemphys.2021.124386.

[44] S. Sun, C. Liu, G. Wang, Z. Chen, T. Chen, R. Peng, Y. Lu, Structural and physical properties of mixed-layer aurivillius-type multiferroics, J. Am. Ceram. Soc. 99 (2016) 3033–3038, https://doi.org/10.1111/jace.14312.

[45] M.I. Morozov, V.V. Gusarov, Synthesis of Am – 1Bi2MmO3m + 3 compounds in the Bi4Ti3O12–BiFeO3 system, Inorg. Mater. 38 (2002) 723–729, https://doi.org/10.1023/A:1016252727831.

[46] Z. Zhang, H. Yan, X. Dong, Y. Wang, Preparation and electrical properties of bismuth layer-structured ceramic Bi3NbTiO9 solid solution, Mater. Res. Bull. 38 (2003) 241–248, https://doi.org/10.1016/S0025-5408(02)01032-2.

[47] K. Qian, L. Xia, W. Wei, L. Chen, Z. Jiang, J. Jing, J. Xie, Construction of Bi2Ti2O7/Bi4Ti3O12 composites with enhanced visible light photocatalytic activity, Mater. Lett. 206 (2017) 245–248, https://doi.org/10.1016/j.matlet.2017.07.036.

[48] C. Jia, Y. Chen, W.F. Zhang, Optical properties of aluminum-, gallium-, and indium-doped Bi4Ti3O12 thin films, J. Appl. Phys. 105 (2009) 113108, https://doi.org/10.1063/1.3138813.

[49] A. Kudo, S. Hijii, H2 or O2 evolution from aqueous solutions on layered oxide photocatalysts consisting of Bi3+ with 6s2 configuration and d0 transition metal ions, Chem. Lett. 28 (1999) 1103–1104, https://doi.org/10.1246/cl.1999.1103.

[50] G. Chen, W. Bai, L. Sun, J. Wu, Q. Ren, W. Xu, J. Yang, X. Meng, X. Tang, C.-G. Duan, J. Chu, Processing optimization and sintering time dependent magnetic and optical behaviors of Aurivillius Bi5Ti3FeO15 ceramics, J. Appl. Phys. 113 (2013) 034901, https://doi.org/10.1063/1.4775800.

[51] X. Zuo, S. Zhu, J. Bai, E. He, Z. Hui, P. Zhang, D. Song, W. Song, J. Yang, X. Zhu, J. Dai, Enhanced multiferroicity and narrow band gap in B-site Co-doped Aurivillius Bi5FeTi3O15, Ceram. Int. 45 (2019) 137–143, https://doi.org/10.1016/j.ceramint.2018.09.144.

[52] W. Bai, W.F. Xu, J. Wu, J.Y. Zhu, G. Chen, J. Yang, T. Lin, X.J. Meng, X.D. Tang, J. H. Chu, Investigations on electrical, magnetic and optical behaviors of five-layered Aurivillius Bi6Ti3Fe2O18 polycrystalline films, Thin Solid Films 525 (2012) 195–199, https://doi.org/10.1016/j.tsf.2012.10.058.

[53] Y. Huang, L. Mi, J. Qin, S. Bi, H.J. Seo, Synthesis, optical, and magnetic properties of six-layered Aurivillius bismuth ferrititanate, J. Am. Ceram. Soc. 102 (2019) 3555–3566, https://doi.org/10.1111/jace.16226.

[54] F. Gao, Y. Yuan, K.F. Wang, X.Y. Chen, F. Chen, J.-M. Liu, Z.F. Ren, Preparation and photoabsorption characterization of BiFeO3 nanowires, Appl. Phys. Lett. 89 (2006) 102506, https://doi.org/10.1063/1.2345825.

[55] S.N. Habisreutinger, L. Schmidt-Mende, J.K. Stolarczyk, Photocatalytic reduction of CO2 on TiO2 and other semiconductors, Angew. Chem. Int. Ed. 52 (2013) 7372–7408, https://doi.org/10.1002/anie.201207199.

[56] M. Yu, Y. Wang, H.-Y. Wang, J. Han, Y. Qin, J.-P. Zhang, X.-C. Ai, The influence of morphology on charge transport/recombination dynamics in planar perovskite solar cells, Chem. Phys. Lett. 662 (2016) 257–262, https://doi.org/10.1016/j.cplett.2016.09.046.

[57] K. Cai, C. Huang, D. Guo, Significantly enhanced piezoelectricity in low-temperature sintered Aurivillius-type ceramics with ultrahigh Curie temperature of 800 °C, J. Phys. Appl. Phys. 50 (2017) 155302, https://doi.org/10.1088/1361-6463/aa5872.

[58] L.D. Zhao, D. Berardan, Y.L. Pei, C. Byl, L. Pinsard-Gaudart, N. Dragoe, Bi1−xSrxCuSeO oxyselenides as promising thermoelectric materials, Appl. Phys. Lett. 97 (2010) 092118, https://doi.org/10.1063/1.3485050.

[59] Key laboratory of chemical utilization of forestry biomass of zhejiang province, zhejiang agriculture and forestry university, hangzhou, zhejiang province, 311300, China, L. Bai, fabrication and photoelectrochemical performances of BiFeO3 thin film photoelectrodes: effect of annealing temperature, Int. J. Electrochem. Sci. (2021) 210721, https://doi.org/10.20964/2021.07.25.

[60] Q. Shao, H. Lin, M. Shao, Determining locations of conduction bands and valence bands of semiconductor nanoparticles based on their band gaps, ACS Omega 5 (2020) 10297–10300, https://doi.org/10.1021/acsomega.9b04238.

[61] S.J.A. Moniz, R. Quesada-Cabrera, C.S. Blackman, J. Tang, P. Southern, P. M. Weaver, C.J. Carmalt, A simple, low-cost CVD route to thin films of BiFeO 3 for efficient water photo-oxidation, J. Mater. Chem. A 2 (2014) 2922–2927, https://doi.org/10.1039/C3TA14824F.